

Elastic Radiation Generated by a Point Explosion in a Breakaway-Glass Plate

Jonathan M. Mihaly^{1*}, Charles G. Sammis², Ares J. Rosakis¹, and Harsha S. Bhat^{1,2†}

¹Graduate Aerospace Laboratories, California Institute of Technology, Pasadena, CA. 91125

²Department of Earth Sciences, University of Southern California, Los Angeles, CA. 90089

Corresponding author: Charles Sammis sammis@usc.edu

*Currently at Jet Propulsion Laboratory, Pasadena, CA. 91109

†Currently at Ecole Normale Supérieure, Paris France.

Key Points:

- Low fracture toughness of break-away glass promotes extensive fracture patterns similar to those observed in underground explosions.
- The generation of fracture damage generates significant additional P wave radiation in excess of that produced directly by the explosion.
- Weak S waves are also observed, which are most likely generated by the asymmetric development of long radial tensile fractures

Abstract

Point explosions were generated in a suite of breakaway-glass plates by the application of a high-voltage pulse to a thin nichrome wire. The resultant elastic waves were recorded by high-speed photography and by laser velocimeters attached to the sample surface. The elastic wave velocities, uniaxial failure strength, and critical stress intensity factor for tensile loading (K_{IC}) were measured independently and used in a dynamical micromechanical damage model to simulate the experiments. The model successfully predicts the observed damage morphology and the waveforms of the resultant elastic radiation. Both the experiments and the numerical model produced a secondary compressional pulse generated by the dilatation associated with the damage and a small shear wave that can be ascribed to asymmetry in the pattern of radial fractures.

Plain Language Summary

An underground nuclear explosion generates seismic waves that can be recorded at great distances. Analysis of this seismic radiation is routinely used to discriminate between explosions and earthquakes and to measure the yield of nuclear events. In principle, discrimination should be simple. The radial motion in explosions should radiate mainly compressional (P) waves while the fault slip in earthquakes should radiate mostly shear (S) waves. In fact, underground explosions are observed to radiate large S waves making them more difficult to discriminate from earthquakes. It has been argued that these S waves may be generated by path effects such as reflection and scattering and by source asymmetry caused by stress in the crust and fracture anisotropy in the rock. One important but poorly understood source effect is the extensive pulverization of rock that occurs just following detonation. Theoretical models predict that asymmetric fracturing can generate S waves, and that it also affects the coupling of explosive energy to seismic radiation, thus affecting the estimate of yield. In this study we measure the seismic radiation from laboratory explosions in plates of break-away glass, which we compare with estimates from a theoretical model for fracture evolution during an explosion. We confirm theoretical predictions that the rock pulverization makes a significant contribution to the radiated P waves and that it generates S waves when the fracture pattern is not spherical.

1 Introduction

In order to prevent nuclear fallout from entering into the atmosphere or oceans, the 1963 Limited Test Ban Treaty banned all nuclear tests except for those performed underground. In 1974, the United States and the Soviet Union signed the Threshold Test Ban Treaty, which banned underground tests with yields greater than 150 kilotons. The need to monitor and enforce this limit has motivated studies of the relationship between explosive yield and apparent seismic magnitude, as well as strategies to discriminate between underground nuclear explosions and earthquakes having the same apparent magnitude. More recently seismic analysis has been extended to the detection and discrimination of smaller underground nuclear tests.

It should be simple to discriminate between underground explosions and earthquakes. Explosions should generate mostly compressional waves while earthquakes should generate mostly shear waves. However, discrimination has turned out to be a difficult problem since underground nuclear explosions are observed to generate relatively large shear waves. Proposed sources of these S waves generally fall into one of two categories: propagation effects or non-linear source effects. In this paper we focus on one particular non-linear source effect: the generation of fracture damage by the explosive pressure wave. Johnson and Sammis (2001)

calculated the elastic radiation from an explosive source in a medium described by the micromechanical damage mechanics formulated by Ashby and Sammis (1990). They found that dilatation associated with the fracture damage generates a P wave with an amplitude roughly 40% of that generated by the explosion. They also found that damage generates strong S wave radiation if the spherical symmetry of the source is broken by either an anisotropic initial fracture distribution or by a regional tectonic shear stress.

The Ashby and Sammis (1990) damage model is quasistatic. It assumes that as the cracks grow, the stress intensity at the crack tips is always at its critical value, which is not the case at the very high loading rates imposed by explosive sources. Deshpande and Evans (2008) and Bhat et al. (2012) modified the Ashby and Sammis (1990) model to incorporate the effects of loading rate on the nucleation and growth of fractures. The Ashby and Sammis (1990) model also assumed compressive loading on the starter flaws. The newer formulations also allow tensile loading, which occurs during the rarefaction phase of the pressure wave (see, e.g., Johnson and Sammis, 2001). Bhat et al. (2012) showed that their model correctly predicts the failure strength of marble over a 14 order of magnitude range of loading rates. In this paper we further test the Bhat et al. (2012) dynamic damage mechanics by using it to simulate the damage and elastic radiation produced by point explosions in brittle plates.

2 Experimental Apparatus

The experimental configuration in Fig. 1 is based on that developed by Mello et al. (2010, 2011, 2012). A 152.4x152.4x4.5 mm plate with an 0.01 inch diameter hole drilled through its center was mounted standing on one edge, with light contact from two roller pins at the upper and lower corners of the right hand vertical edge (Fig. 2). Illumination from a collimated laser was imaged by two Cordin gated, intensified high-speed cameras with 50 ns exposure times. A 76 μ m (3 mil) diameter nichrome wire was threaded through the hole and attached to a bank of capacitors. Discharge of the capacitors exploded the wire and triggered the high-speed cameras. Three Poltytec velocimeters provided point measurements of one component of the velocity at the three locations indicated in Figs. 2 and 3.

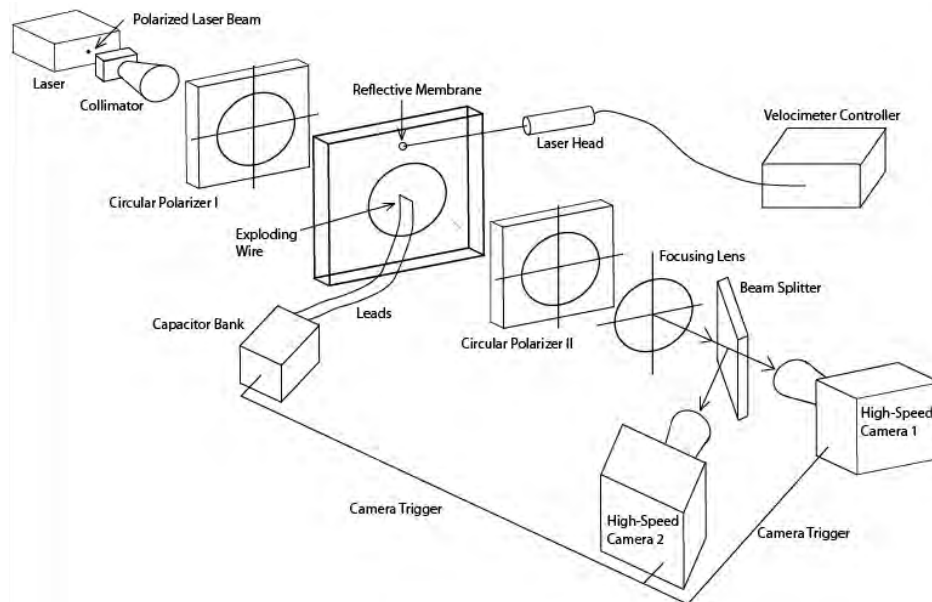


Figure 1. Schematic diagram of experimental configuration. The fracture damage and associated elastic radiation generated by an exploding wire in a breakaway-glass plate are illuminated by collimated laser light and recorded using high speed cameras and laser velocimeters.

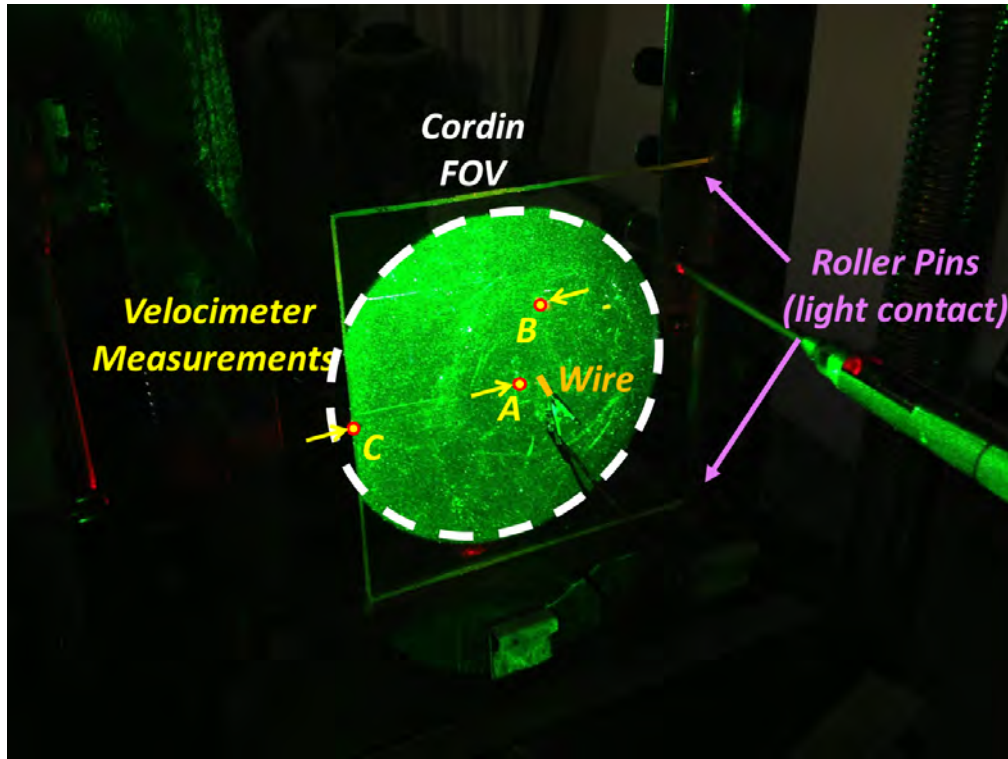


Figure 2. Sample before an explosion showing the three sensor locations and component of motion measured by each. Note sensors A and C record radial motion while sensor B records transverse motion.

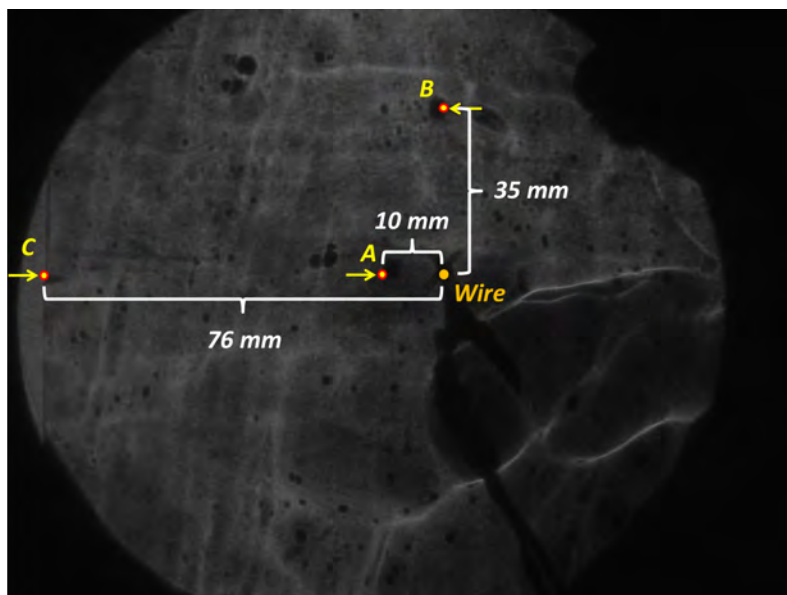


Figure 3. Photo of a sample before the explosion showing the placement of laser sensors. The illuminated circle is the field of view of the high-speed Cordin cameras as indicated by the white dashed circle in Fig. 2. This photo was taken using Polaroid filters that reveal small-scale heterogeneity in the sample.

3 Experimental Samples

Plates of breakaway-glass were used in this investigation. Sometimes called “candy-glass”, this material is used to simulate silica glass in movie stunts. While, as the name implies, it was originally a sugar glass, the industry now uses a polymer, the composition of which is a trade secret. Given the unknown composition and the fact that we could find no measurements of physical properties in the literature, we measured the elastic wave velocities, the uniaxial stress-strain curve to failure, and the critical stress intensity factor for tensile loading K_{IC} of our sample material. These properties, which are required inputs for the micromechanical damage mechanics modeling presented in a later section, are summarized in Table 1. Details of their measurement are given in Appendix A.

Table 1. Physical properties of breakaway glass samples

Property	Symbol	Value	Units
Density	ρ	1041	Kg/m ³
P wave velocity	v_P	2162 ± 18	m/s
S wave velocity	V_{S1}	1116 ± 7	m/s
S wave velocity	V_{S2}	1051 ± 21	m/s
Poisson's ratio	ν	0.332 ± 0.005	
Critical stress intensity factor	K_{IC}	0.0156 ± 0.0007	MPa/m ^{1/2}
Dominant flaw size	a	8.2×10^{-6}	m
Initial damage	D_0	0.13	
Flaw density	N_V	1.58×10^{14}	flaws/m ³

Table 2 compares mechanical properties of breakaway-glass with Homalite -100, fused quartz, and Westerly granite. Homalite -100 is the photoelastic polymer that is commonly used to image shear stress concentrations associated with dynamic rupture (see, e.g., Xia et al., 2004). Note that the elastic velocities in breakaway-glass are comparable to those in Homalite-100 but the critical stress intensity factor K_{IC} is more than an order of magnitude smaller. It is this very low K_{IC} in breakaway-glass that makes it useful in movie stunts and allows the production of complex fracture patterns in the relatively low pressure field generated by the exploding wire.

Table 2. Comparison between the mechanical properties of breakaway glass and other materials.

Material	V_p (m/s)	V_s (m/s)	Density (kg/m ³)	Poisson's ratio	K_{IC} (MPa/m ^{1/2})
Breakaway Glass	2162	1116	1041	0.32	0.0156
Homalite – 100	2498	1200	1230	0.35	0.6
Fused Quartz	5900 - 6200	3900 – 4200	2230	0.1	0.85 – 1.0
Granite	5500	3200	2540	0.24	1.0

4 Experimental Results

Figures 3 through 6 show selected high-speed Cordin images before, during and after an explosion. Figure 7 shows a post-test image of the sample. Next to it is the fracture pattern produced by a nuclear explosion as revealed by fracture mapping in mine shafts and boreholes (Bishop, 1963). Note that the laboratory explosion produces the main morphological characteristics of the nuclear explosion: extensive fragmentation close to the source and longer isolated radial fractures.

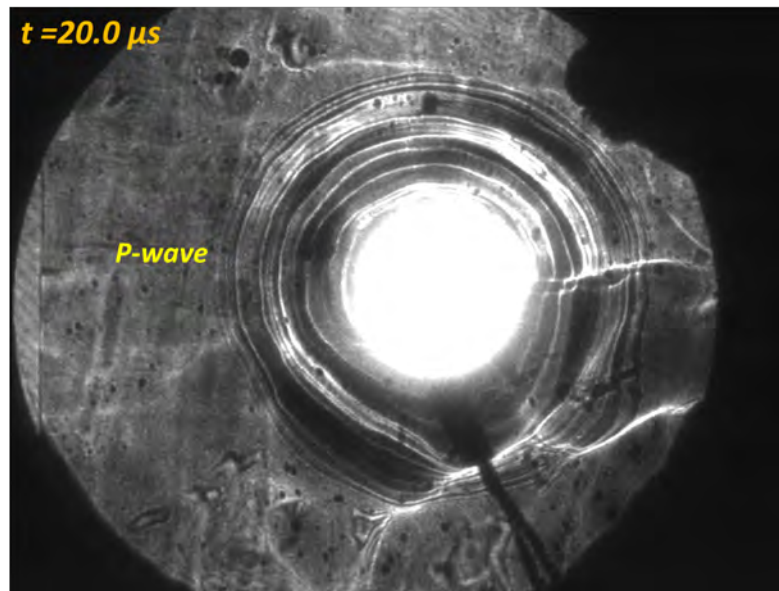


Figure 4. Image of the sample 20.0 μ s after the explosion. The flash from the explosion is evident. The breakaway-glass has a sufficiently large photoelastic constant to reveal the P wave, which has moved 40 mm in 20 μ s, or 2000 m/s, which is slightly below the average P wave velocity that was measured ultrasonically to be 2162 m/s (see Appendix A). The left edge of the plate is also visible.

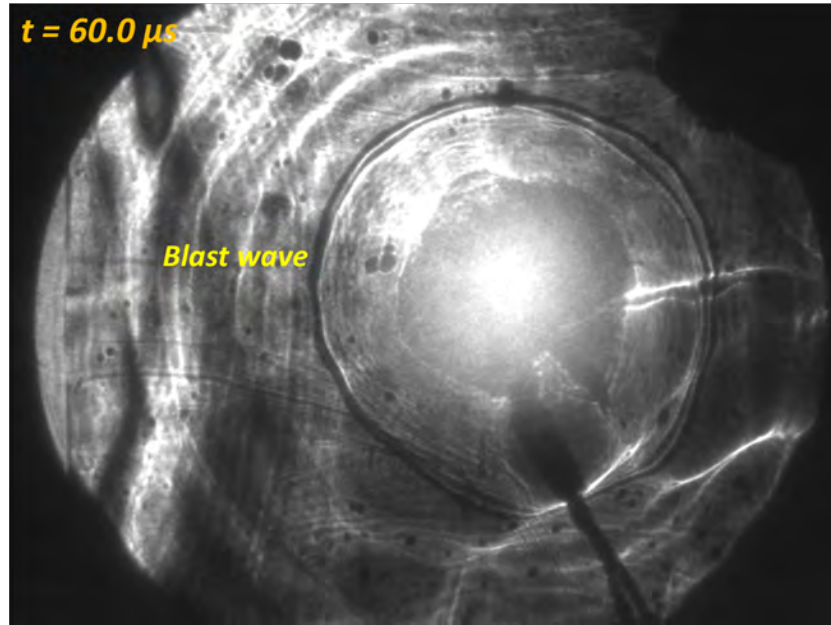


Figure 5. Image of the sample 60.0 μs after the explosion. The flash from the explosion is still visible as is a debris cloud that, unfortunately, hides the emerging fracture pattern. The thin dark circle is the acoustic blast wave that is traveling at the speed of sound in air. P waves reflected from the left edge are also visible

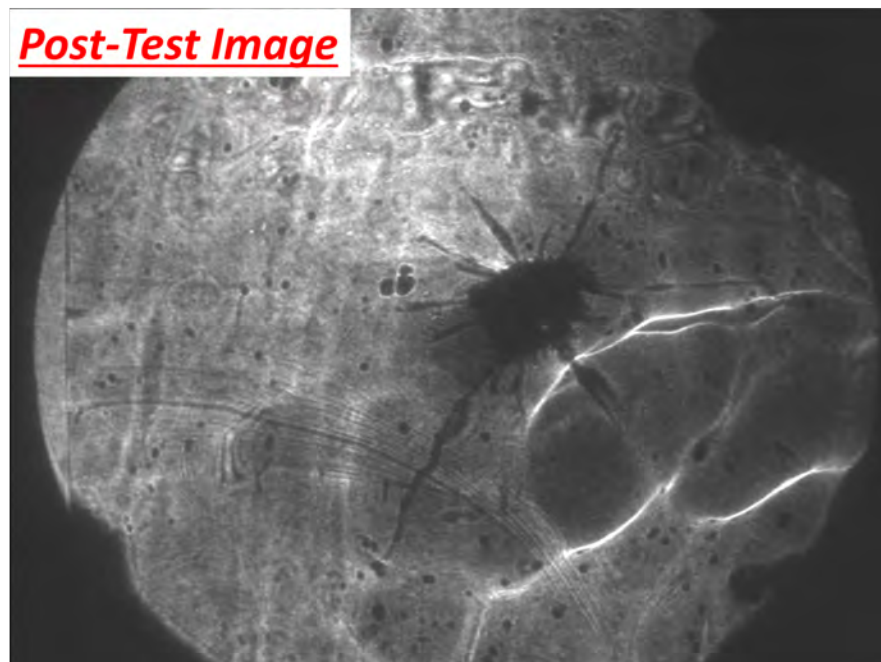


Figure 6. Image of the sample at the end of the experiment showing the fracture pattern.

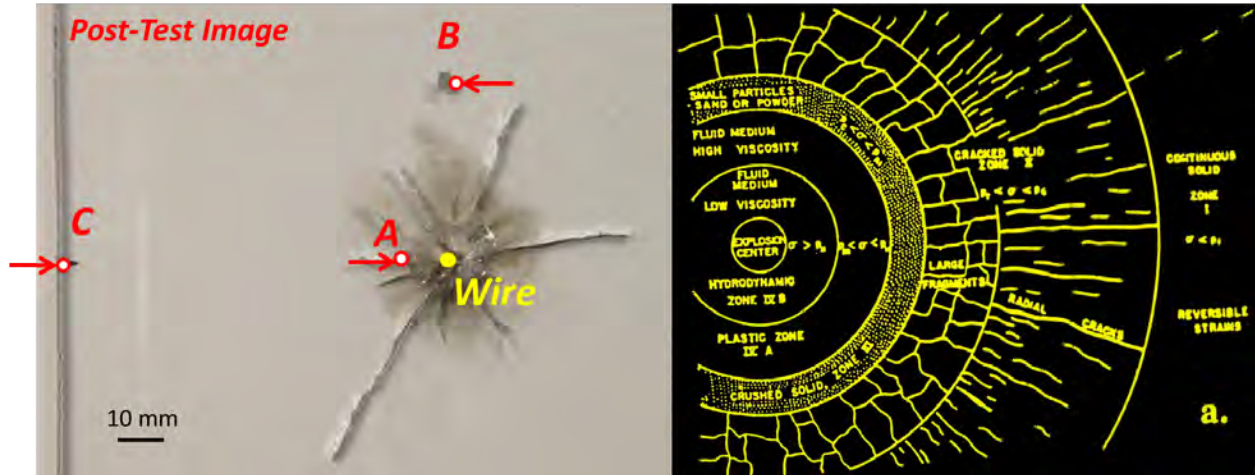


Figure 7. Comparison of the experimental fracture pattern with that produced by an underground nuclear explosion. Both patterns are characterized by radial and circumferential cracking that pulverizes the material close to the explosion and a set of radial cracks that extend well beyond the circumferential cracks. Note that reflector (A) lies within the pattern of circumferential fractures.

P waves emitted from the exploding wire are observable as caustic fringes in Fig. 4 taken 20 μs after trigger. Reflections of these waves from the left edge of the sample are observed in Fig. 5 captured at 60 μs . The slower air blast wave produced by the exploding wire is also observed in Fig. 5.

Figures 8 and 9 show the signals from the three laser velocimeters in experiments #1 and #2 respectively. The upper trace from the sensor at location (A) shows a double peak structure in both experiments. Our interpretation is that the first peak is the P wave arrival while the second peak is the arrival of the damage front, which Johnson and Sammis (2001) showed travels at a velocity between V_P and V_S .

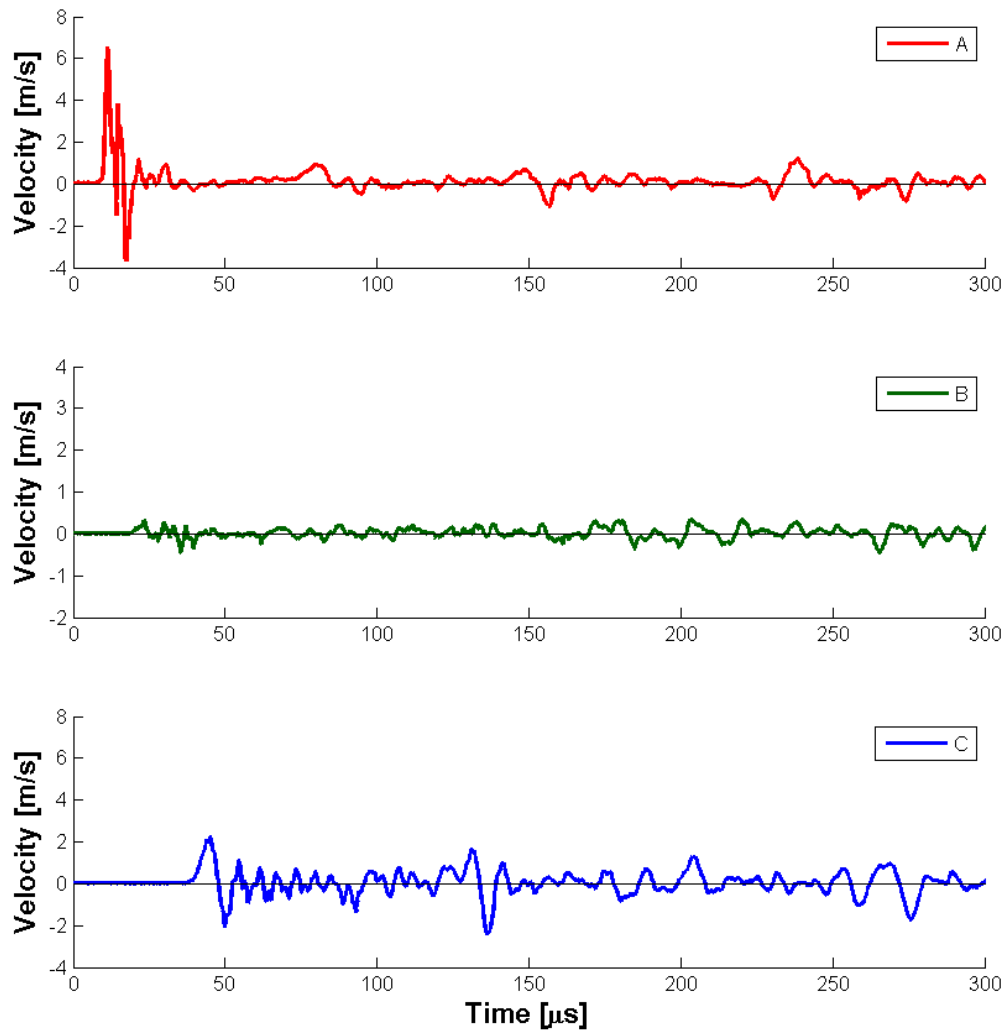


Figure 8. Recordings of the x component of velocity from experiment #1 recorded at the three stations indicated in Fig. 2. Stations A and C recorded radial velocity. Station B recorded transverse velocity (see Fig. 3).

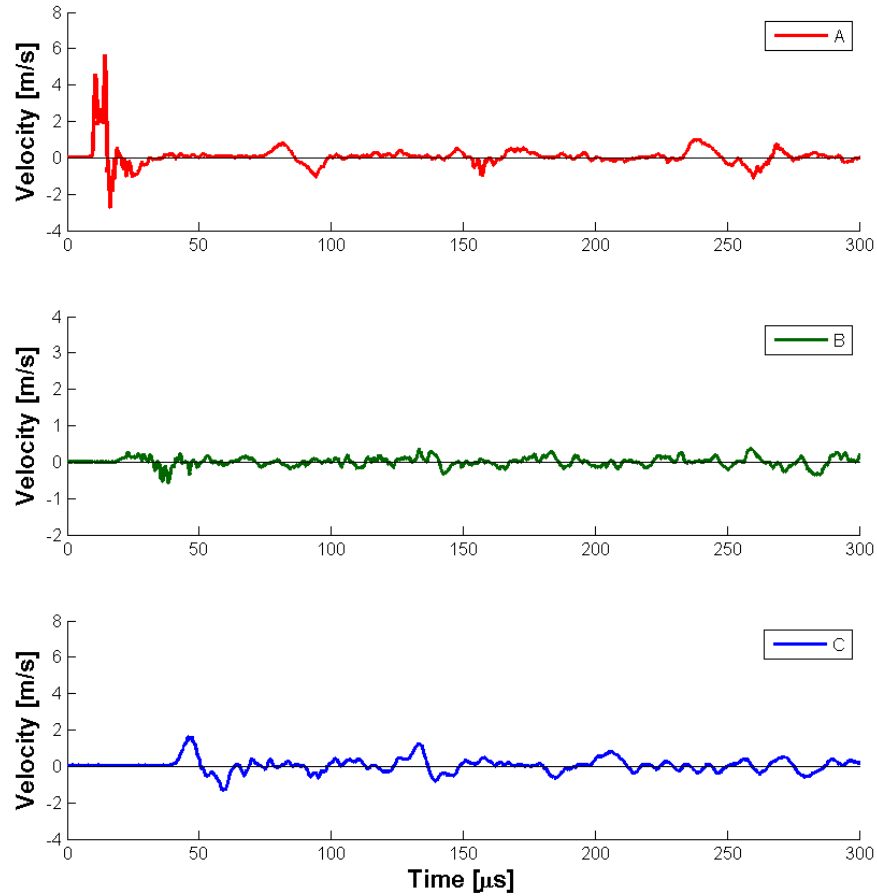


Figure 9. Recordings of the x component of velocity from experiment #2, which used the same station configuration as experiment #1 as indicated in Figs 2 and 3. Note the repeatability of the experiment. Also note that both records have a large initial double peak at station A.

Figure 10 shows the travel paths of the arrivals plotted on the travel time curves in Figs. 11 and 12. The time delay of 55 μsec across the 10 mm damage zone experienced by R1, R2, and L4 can be used to estimate the damage in the heavily damaged zone near the explosion. This delay corresponds to a ratio of damaged to undamaged velocities of $v_d / v = 0.144$, which, using O'Connell and Budianski (1974), corresponds to $N_v \langle a^3 \rangle = 0.55$, which in turn corresponds to a

damage (in the Bhat et al. (2012) damage mechanics) of $D = \frac{4}{3} \pi N \langle a^3 \rangle = \frac{4}{3} \pi 0.55 = 2.3$. Since

we stop damage accumulation in our simulations at $D=1$, we underestimate the effects of damage in the simulations. Modeling post-failure damage accumulation and the associated deformation remains a major unsolved problem in theoretical damage mechanics.

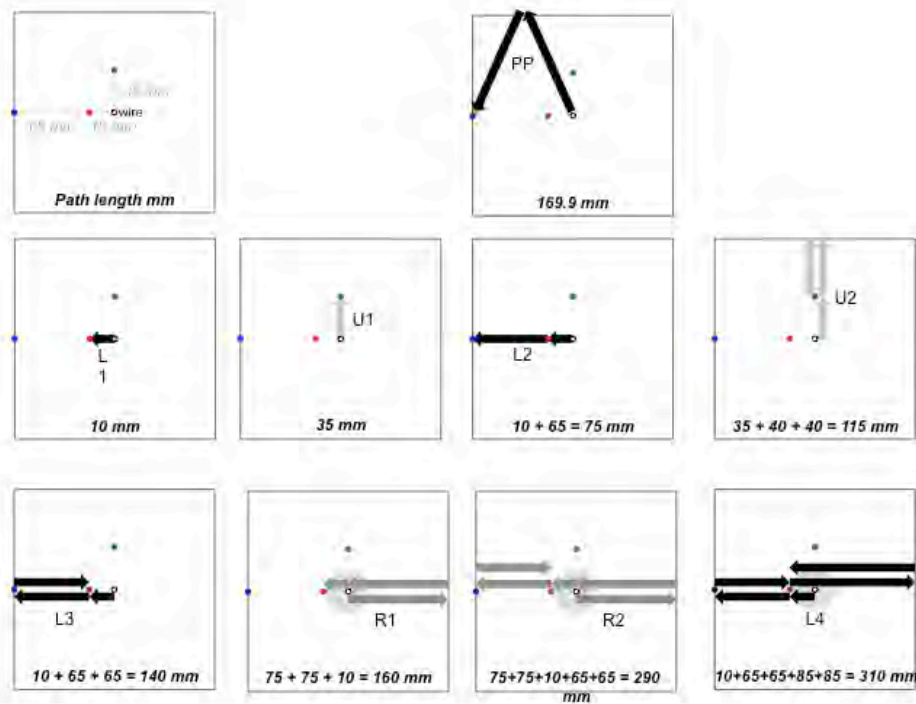


Figure 10. Travel paths for the arrivals plotted on travel time curves in Figs. 11 and 12. Note that R1, R2, and L4 pass through the damage zone producing delayed arrivals. The slowness through the damage zone can be used to calculate the total damage.

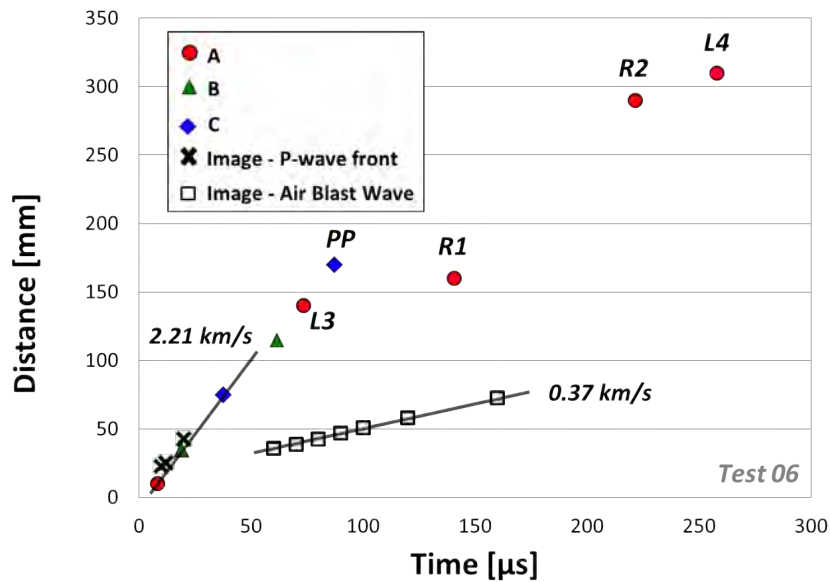


Figure 11. Travel time curves for experiment #1 (seismograms in Fig. 8). Note that the P wave and air blast wave are easily identified. Arrivals R1, R2, and L4 are delayed by passage through the damage zone. Note also that the velocities measured from the high-speed images are consistent with those from the velocimeter stations measured using linear regression.

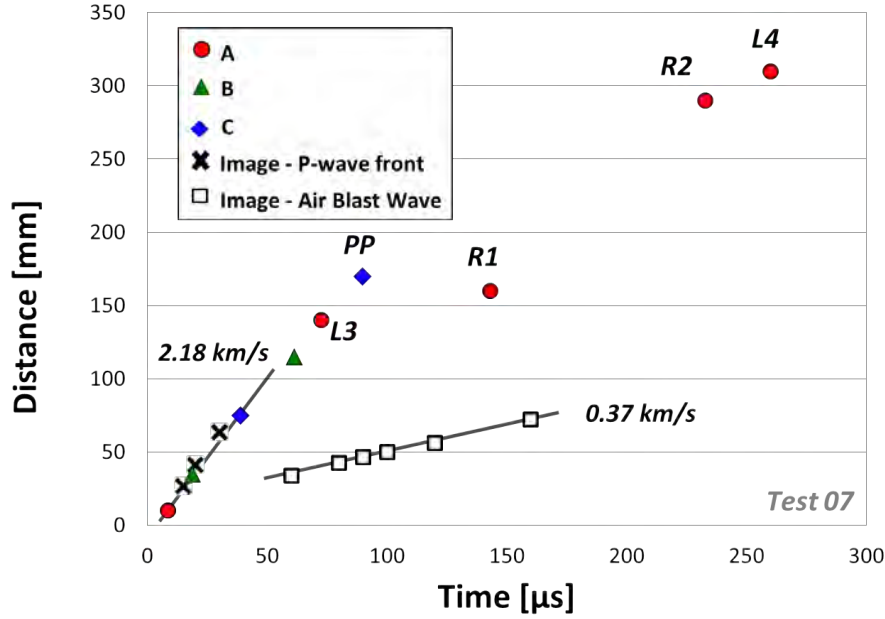


Figure 12. Travel time curves for experiment #2. Note the consistency with experiment #1 in Fig. 11.

5 Micromechanical Modeling of Experimental Results

We simulated the experimental results in the previous section using the dynamic micromechanical damage mechanics formulated and implemented as a user defined rheology in the ABAQUS dynamic finite element code by Bhat et al. (2012).

5.1 Dynamic micromechanical damage mechanics

The Ashby and Sammis (1990) and Bhat et al. (2012) formulations assume that the material has a homogeneous initial distribution of randomly oriented penny-shaped fractures all having the same radius a . For any local stress field characterized by a largest principal stress σ_1 and a smallest principal stress σ_3 , only those cracks that are optimally oriented for sliding in shear are activated and nucleate tensile wing-cracks at their tips as in Fig. 13. For a volume density N_V of such optimally oriented cracks, the initial damage is defined as $D_0 = \frac{4}{3}\pi N_V(\alpha a)^3$, where $\alpha = \cos(\Psi)$ and Ψ is the angle between the optimal cracks and σ_1 as in Fig. 13. As the applied stress increases, the length l of the wing cracks increases as does the damage defined as $D = \frac{4}{3}\pi N_V(l + \alpha a)^3$. The growing wing cracks interact to enhance each other's growth, which ultimately leads to unstable growth and macroscopic failure.

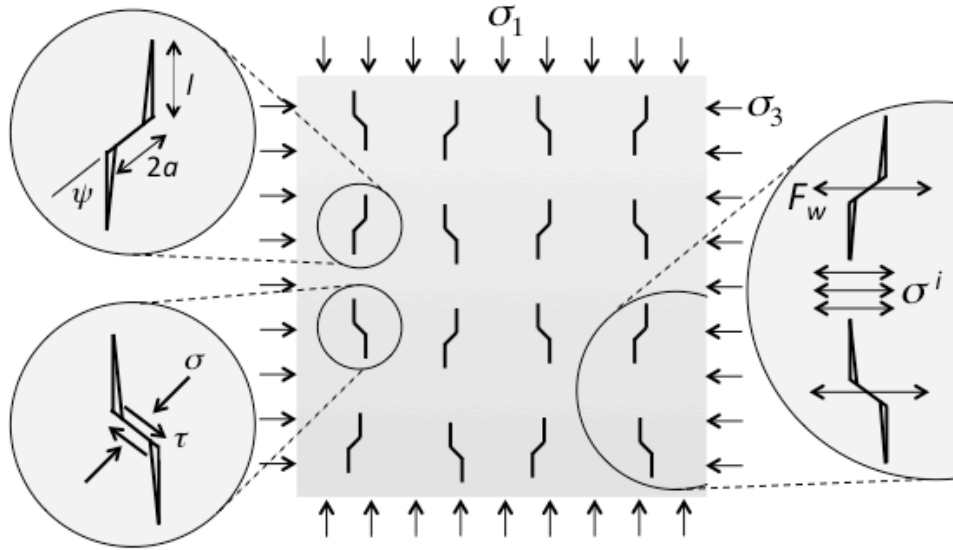


Figure 13. Geometry in the micromechanical damage mechanics model. Sliding on an array of penny-shaped cracks having volume density of N_V and radius a produces a wedging force F_w that drives tensile wing cracks to open in the direction of the smallest principal stress σ_3 and propagate parallel to the largest principal stress σ_1 . Growth of wingcracks is enhanced by σ_1 , retarded by σ_3 , and enhanced by a global interaction that produces a mean tensile stress $\sigma^{(i)}$. The positive feedback provided by this tensile interaction stress leads to a run-away growth of the wing cracks and ultimate macroscopic failure.

5.2 Input Parameters for breakaway-glass

The mechanical properties of breakaway-glass that are required inputs to the damage mechanics are summarized in Table 1. The size a and density N_V of starter flaws in the candy glass were determined from the uniaxial stress-strain curve as detailed in the Appendix. The elastic moduli and critical stress intensity factor were measured directly. Since we have no data for breakaway-glass at high loading rates, we used the parameters for glass from Bhat et al. (2012) to characterize the increase in critical stress intensity at high loading rates.

5.3 Finite element mesh

The 152x152 mm experimental plates were modeled in 2D using the ABAQUS finite element code. Triangular elements were automatically generated from 1 mm node seeds. The central wire was modeled as a 1 mm diameter hole in the center of the plate with the pressure source time function applied to its interior element edges.

5.4 The source time function

The amplitude, duration, and rise-time of the pressure source were selected such that the peak amplitude and duration of the simulated pulse at station A were consistent with experimental observations. For the fit shown in Fig. 14 the exploding wire was modeled as a 50 MPa pressure pulse with 4 μ s duration and 0.1 μ s rise and fall times. Note that the second pulse is larger in the experiment than in the model. This may be a consequence of the fact that our

simulation only allows a maximum damage value of $D=1.0$ while the damage estimated in a previous section from the travel time delay is $D=2.1$. The extra dilatation associated with the extra damage could explain the larger second pulse in the experiment.

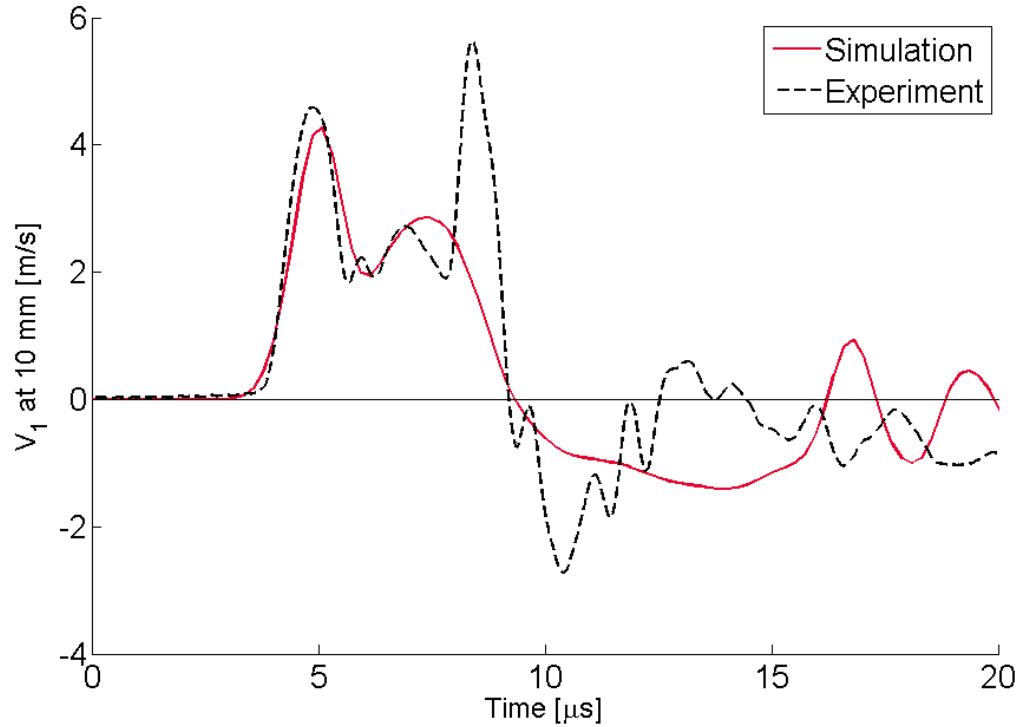


Figure 14. Comparison of the radial velocity measured at station A in experiment #2 with the finite element simulation. In the simulation, the exploding wire was modeled as a 50 MPa pressure pulse with 4 μs duration and 0.1 μs rise and fall times.

5.5 Post-test fracture pattern

The post-test fracture pattern for the simulation in Fig. 14 is shown in Fig. 15 where it is compared with the sample. The model accurately simulates the extent of the pulverized zone close the explosion and the length of the longer radial fractures.

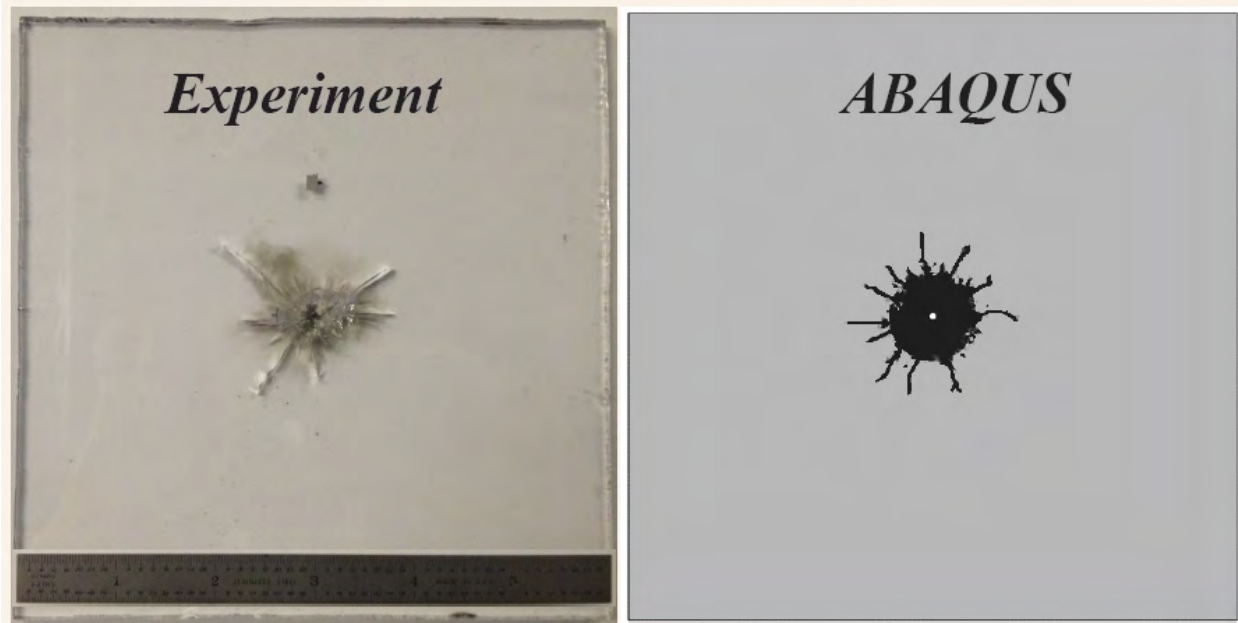


Figure 15. Comparison of the simulated and experimentally produced fracture patterns. The black area in the simulation indicates $D=1$, the maximum damage allowed in our model.

5.6 Isochromats and particle motions

Numerically generated isochromats for Mises stress in Fig. 16 can be compared with the high-speed images produced in the experiments. A similar fringe pattern is observed. Uniform node velocity vectors (showing direction but not amplitude) are superimposed on the theoretical isochromats in Fig. 16. Both longitudinal (P wave) and transverse (S-wave) particle motions are observed.

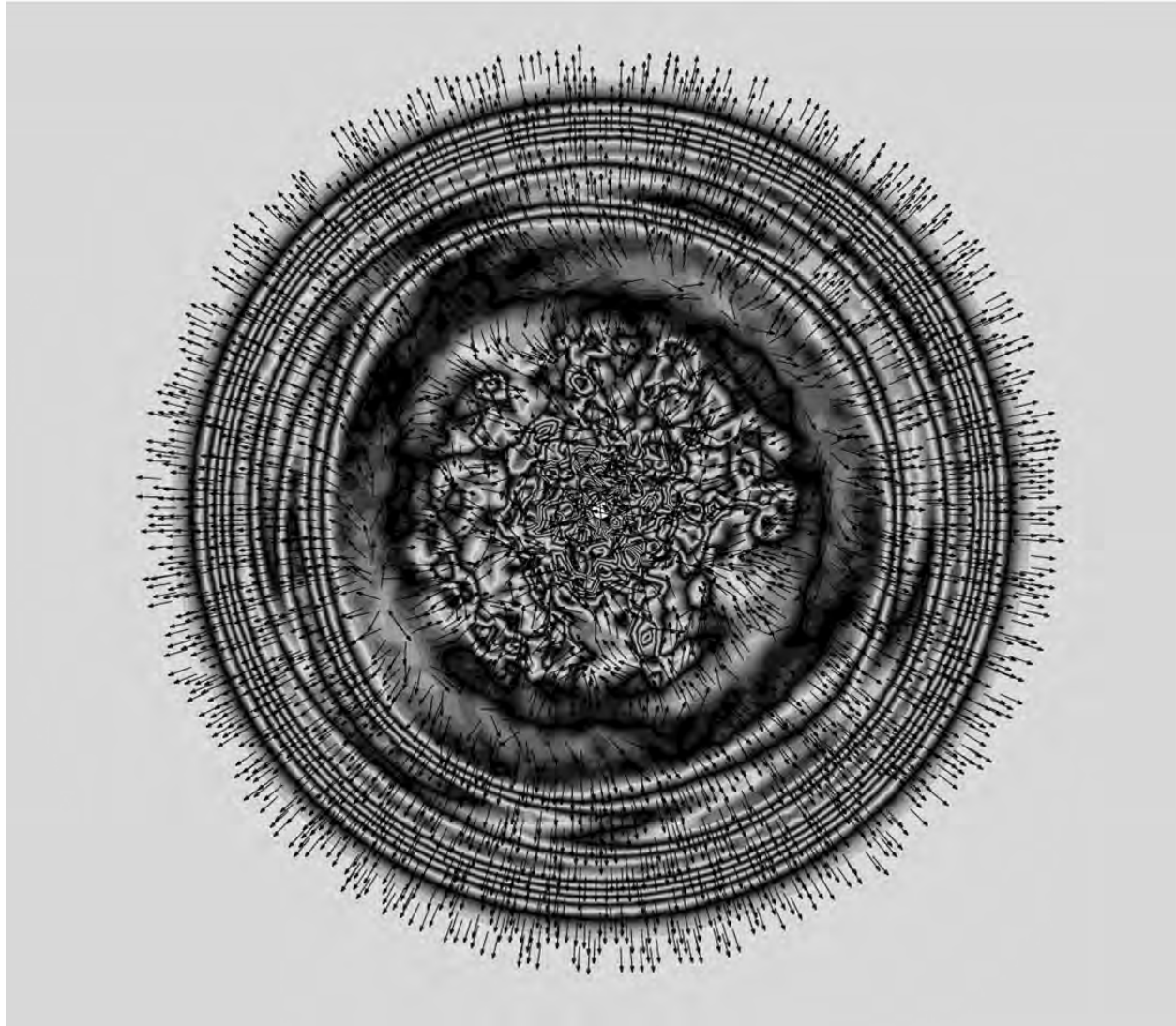


Figure 16. Numerically produced isochromats for Mises stress for comparison with the high-speed images produced in experiments. A similar fringe pattern is observed. Velocity vectors at the nodes are superimposed on the isochromats. Both longitudinal (P wave) and transverse (S wave) particle motions are observed. The velocity vectors are unit vectors denoting direction but not relative amplitude.

5.7 S wave radiation

A second sensor was co-located at station A to record transverse motion. The radial and transverse motions are plotted in Fig. 17. The radial motion shows the typical multipeak waveform for P. The transverse motion shows a weak P arrival followed approximately $4 \mu\text{s}$ later by a stronger S arrival. This is the expected time interval between P and S arrivals at a distance of 10 mm for the velocities in Table 1.

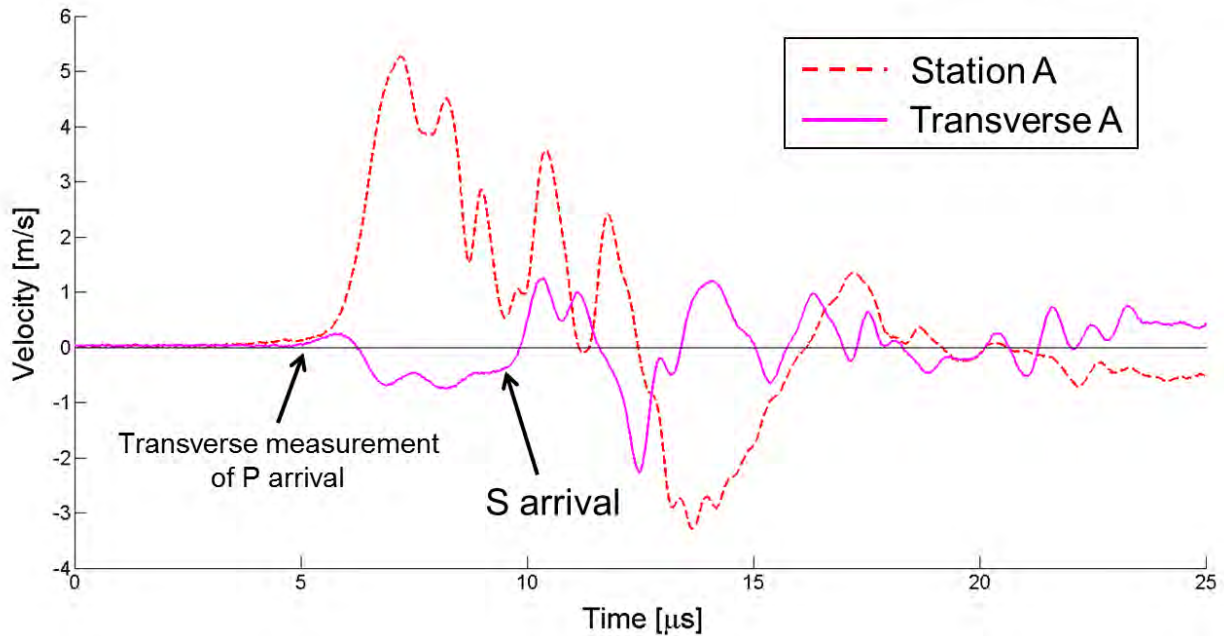


Figure 17. Radial motion (dashed line) and transverse motion (solid line) at station A. Note the strong S wave that arrives on the transverse component about 4 ms after the P wave.

5.8 Secondary P wave radiation

To test our hypothesis that the second large peak in the P waveform is generated by dilatation associated with evolving damage, we ran two computer simulations having identical parameters except for K_{IC} . The first used the value of K_{IC} measured for the breakaway-glass while the second used a very large K_{IC} such that no additional damage was generated by the explosion. Comparison of these two simulations in Fig. 18 shows that the secondary peak in the P waveform was simulated in the first calculation which generated damage but was absent in the second which did not, thus demonstrating that the second P wave peak is due to dynamically generated damage. Figure 19 shows the particle motions associated with the two simulations in Fig. 18. Note that transverse particle motion was produced in the outgoing wave field for the case where damage was generated, but that particle motions were all radial (pure P waves) for the case where no damage was generated.

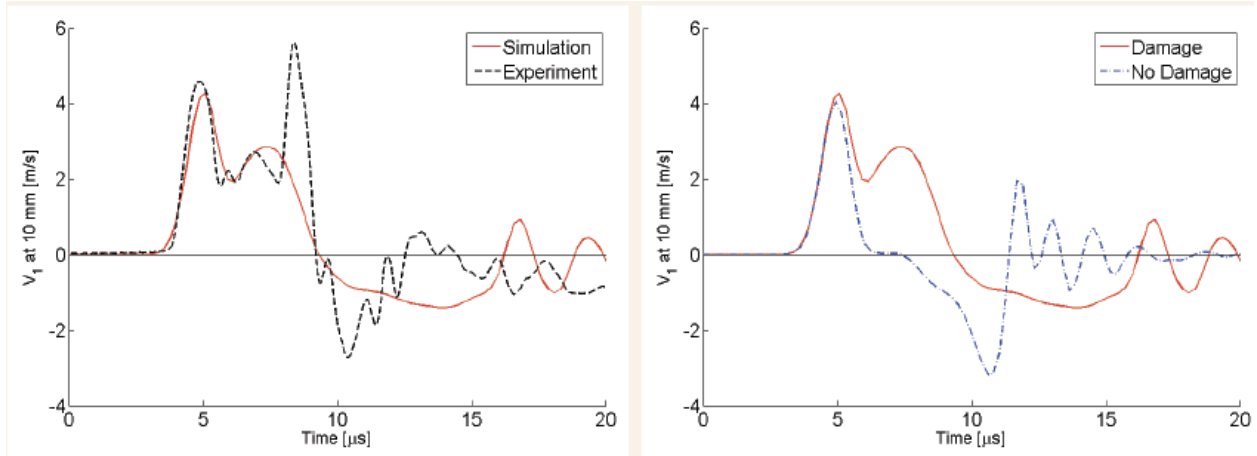


Figure 18. The left panel compares the experiment with a numerical simulation as in Fig. 14. The right panel compares the simulation in the left panel with an identical simulation in which K_{IC} has been increased such that no damage is generated. When no damage is generated, the second peak is absent from the P waveform.

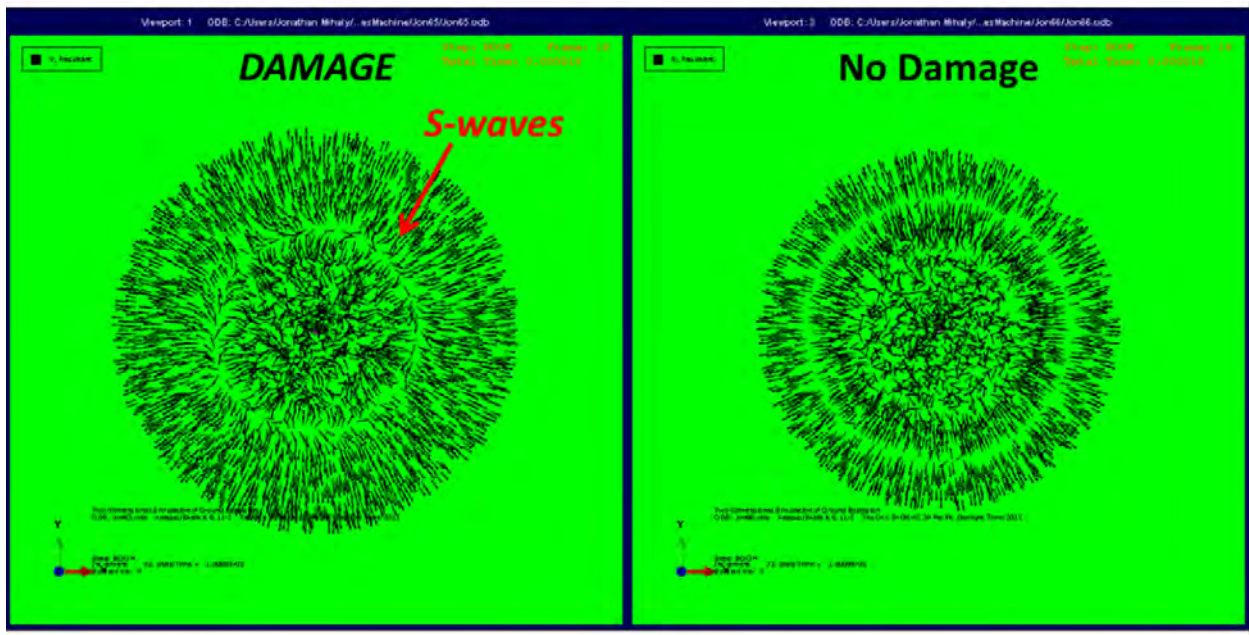


Figure. 19. Particle motion vectors for the two simulations in Fig. 18. Note that the left panel in which damage was generated produced transverse motion in the outgoing wave field while the right panel in which no damage was generated produced only radial motion. The vectors are unit vectors indicating the direction but not relative amplitudes of the particle motions.

6 Discussion

It is interesting that these experiments produced strong S waves in the near field. Organized transverse particle motion is apparent in the theoretical isochromat in Fig. 16, in the experimental velocity seismograms in Fig. 17 and in the velocity field in Fig. 19. Although prior

simulations by Johnson and Sammis (2001) demonstrated that S radiation should be expected when spherical symmetry is broken by pre-stress or fracture anisotropy, neither is present in the experiments reported here. Our best guess is that S waves are generated by asymmetry in the distribution of radial cracks, which is apparent in Figs. 7 and 15. It is an open question whether these S waves will propagate to the far field.

It is also interesting that the P waveforms in the experiments had strong second peaks. This “secondary P pulse” was observed in simulations by Johnson and Sammis (2001) who ascribed it to dilatation associated with the damage. The damage mechanics model used in this paper also produced secondary P waves, which were shown to be a direct consequence of the dynamic damage.

Acknowledgments

The authors thank Vahe Gabuchian and Mike Mello for their assistance with the experimental equipment and Peter Boyd at New England Research for measuring the elastic properties of the break-away glass samples. The digital images and laser velocimeter records are archived at the Caltech Graduate Aerospace Laboratories and are available upon request. This work was supported by Air Force Research Laboratory contract FA9453-12-C-0210.

References

- Ashby, M. F., & Sammis, C. G. (1990), The damage mechanics of brittle solids in compression. *Pure Appl. Geophys.*, 133(3), 489–521.
- Bhat, H. S., Rosakis, A.J., & Sammis, C. G. (2012), A micromechanics based constitutive model for brittle failure at high strain rates. *J. Appl. Mech.*, 79(3), 031016, doi:10.1115/1.4005897. <http://dx.doi.org/10.1115/1.4005897>
- Bhat, H. S., Sammis, C. G., & Rosakis, A. J. (2011), The micromechanics of Westerley granite at large compressive loads. *Pure and Appl. Geophys.*, 168, 2181-2198, <http://dx.doi.org/10.1029/JB079i035p05412>
- Bhat, H. S., Biegel, R. L., Rosakis, A. J., & Sammis, C. G. (2010), The effect of asymmetric damage on dynamic shear rupture propagation II: With mismatch in bulk elasticity. *Tectonophysics*, <http://dx.doi.org/10.1016/j.tecto.2010.03.016>
- Biegel, R. L., Bhat, H. S., Sammis, C. G., & Rosakis, A. J. (2010), The effect of asymmetric damage on dynamic shear rupture propagation I: No mismatch in bulk elasticity, *Tectonophysics*, <http://dx.doi.org/10.1016/j.tecto.2010.03.020>
- Bishop, R. H. (1963), Spherical shock waves from underground explosions, close-in phenomena of buried explosions, *Final Rept. SC-4907(RR) Sandia Corporation*, 115- 158.
- Deshpande, V. S., & Evans, A. G. (2008), Inelastic deformation and energy dissipation in ceramics: A mechanism-based constitutive model, *J. Mech. Phys. Solids*, 56(10), 3077–3100.
- Johnson, L. R., & Sammis, C. G. (2001), Effects of rock damage on seismic waves generated by explosions, *PAGEOPH*, 158, 1869-1908.
- Mello, M. (2012), Identifying the Unique Ground Motion Signatures of Supershear Earthquakes: Theory and Experiments, *Caltech Doctoral Thesis*.

O'Connell, R. J. & Budiansky, B. (1974), Seismic velocities in dry and saturated cracked solids, *Journal of Geophysical Research*, 79, (35), <http://dx.doi.org/10.1007/s00024-011-0271-9>.

Xia, K. W., A. J. Rosakis, A. J., & Kanamori, H. (2004), Laboratory earth-quakes: The sub-Rayleigh-to-supershear rupture transition, *Science*, 303, 1859-1861.

Appendix: The Mechanical Properties of Break-Away Glass

The breakaway-glass used in these experiments was supplied as 4.4 mm thick square plates 152.4 mm on an edge by Alfonso's Breakaway Glass in Burbank, California. Since its composition is a trade secret and we could find no measurements of its physical properties we measured the parameters required as inputs to our damage mechanics model. The parameters found in this appendix are summarized as Table 1 in the body of the paper.

A.1 The density and elastic constants of breakaway glass.

The bulk density of the samples was 1.041 gm/cm^3 . The elastic wave velocities were measured by Peter Boyd at New England Research using a 200 kHz ultrasonic reflection technique. The results are summarized in Table A1.

Table A1. Ultrasonic velocities measured at the four locations on a sample plate. Particle motions for all shear waves are parallel to the plate surface but velocities V_{S1} and V_{S2} have orthogonal particle motions. The values of V_P vary by 2%, V_{S1} by 2%, and V_{S2} by 4% indicating mild heterogeneity. $V_{S1} \neq V_{S2}$ indicating about 5% anisotropy. Note that Poisson's ratio is $\nu \approx 1/3$ typical of metals. Rocks and ceramics tend to have $\nu \approx 1/4$.

Site (Fig. A1)	Thickness	V_P	V_{S1}	V_{S2}	Young's modulus	Poisson's Ratio
	(mm)	(m/s)	(m/s)	(m/s)	(GPa)	
1	4.80	2173	1127	1075	3.35	0.327
2	4.78	2156	1113	1057	3.26	0.330
3	4.47	2179	1110	1048	3.24	0.338
4	4.47	2138	1115	1024	3.17	0.333
Average		2162 ± 18	1116 ± 7	1051 ± 21	3.26 ± 0.07	0.332 ± 0.005

A.2 The critical stress intensity factor for tensile loading of break-away glass.

Figure A1 shows the 4 point bending geometry used to measure K_{Ic} . For our apparatus $d_1 = 25.4 \text{ mm}$ and $d_2 = 37.3 \text{ mm}$. Plate thickness was $w = 4.6 \text{ mm}$. Crack length a , sample height b , and the load at failure P_{fail} are given in Table A2.

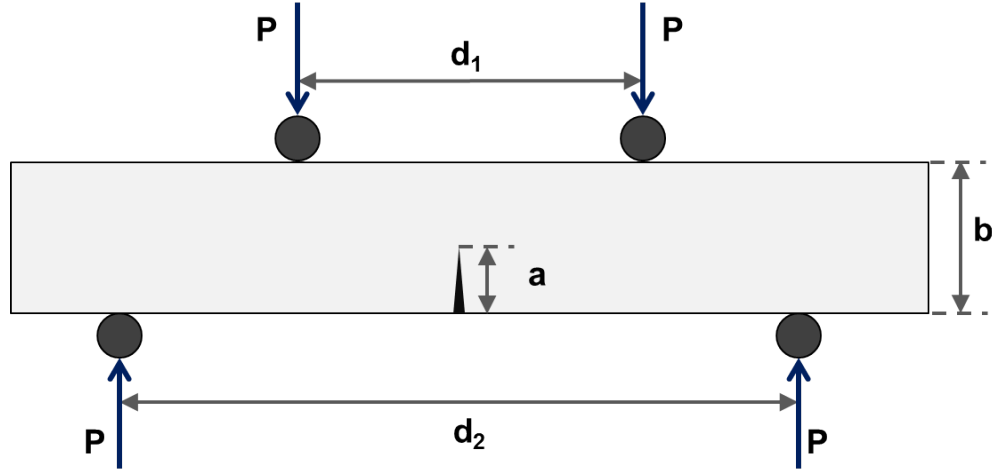


Figure A1. Geometry of four point bending test used to measure K_{IC} .

The critical stress intensity factor was calculated using

$$K_{IC} = \frac{3P(d_2 - d_1)\sqrt{a}}{wb^2} f\left(\frac{a}{b}\right) \quad (A1)$$

where $f\left(\frac{a}{b}\right) = 1.99 - 2.47\left(\frac{a}{b}\right) + 12.97\left(\frac{a}{b}\right)^2 - 23.17\left(\frac{a}{b}\right)^3 + 24.80\left(\frac{a}{b}\right)^4$.

Values of K_{IC} for 3 samples are given in Table A2.

Table A2. Sample parameters in Fig. A2 and values of K_{IC} calculated using eqn. (A1).

	a [mm]	b [mm]	a/b	P_{fail} [N]	K_{IC} [$Pa \cdot m^{1/2}$]
Specimen 3	5.4	18.4	0.294	22.03	16,384
Specimen 4	4.8	18.1	0.265	20.86	15,116
Specimen 5	6.5	18.4	0.353	16.97	15,300
Average					$15,600 \pm 685$

A3. The uniaxial fracture strength of breakaway glass

The micromechanical damage mechanics that we used to model the experiments requires an estimate of the size a and density N_V of the dominant flaws in the sample. These can be estimated from a uniaxial stress-strain curve (at low loading rate) as prescribed in Ashby and Sammis (1990). Figure A2 shows the stress-strain curves to failure for two 38.1 x 19.1 x 4.8 mm rectangular prisms loaded in uniaxial compression as indicated in the inset. The loading rate was

0.25 mm/min. Note that the sample which corresponds to the dashed curve to the right has a slightly larger initial damage ($D_0 = \frac{4}{3}\pi N_V(\alpha a)^3$) as evidenced by the slightly lower modulus and lower failure strength.

The flaw size a was determined by the initiation of damage (first non-linearity in the stress-strain curve) using the expression (from Ashby and Sammis, 1990)

$$\sigma_1^* = \frac{\sqrt{3}}{(1+\mu)^{1/2}-\mu} \frac{K_{IC}}{\sqrt{\pi a}} \quad (\text{A2})$$

where σ_1^* is the stress at which nonlinearity is first observed, $\mu=0.6$ is the coefficient of friction, and K_{IC} is the critical stress intensity factor (which we determined in section A.2 to be $K_{IC} = 1.56 \times 10^4 \text{ Pa m}^{1/2}$). Note that the stress strain curves are linear up to the failure stress in Fig. A2. This occurs when a sample fails as soon as damage nucleates, which implies a relatively high initial flaw density. The above equation gives an initial flaw size of $a = 8.2$ microns.

The initial damage $D_0 = \frac{4}{3}\pi N_V(\alpha a)^3$ was determined by the failure stress (the maximum value of the stress-strain curve in Fig. A2) which turns out to be $D_0 = 0.13$. Since $D_0 = \frac{4}{3}\pi N_V(\alpha a)^3$, D_0 and a give an initial flaw density of $N_V = 1.58 \times 10^{14} \text{ flaws/m}^3$.

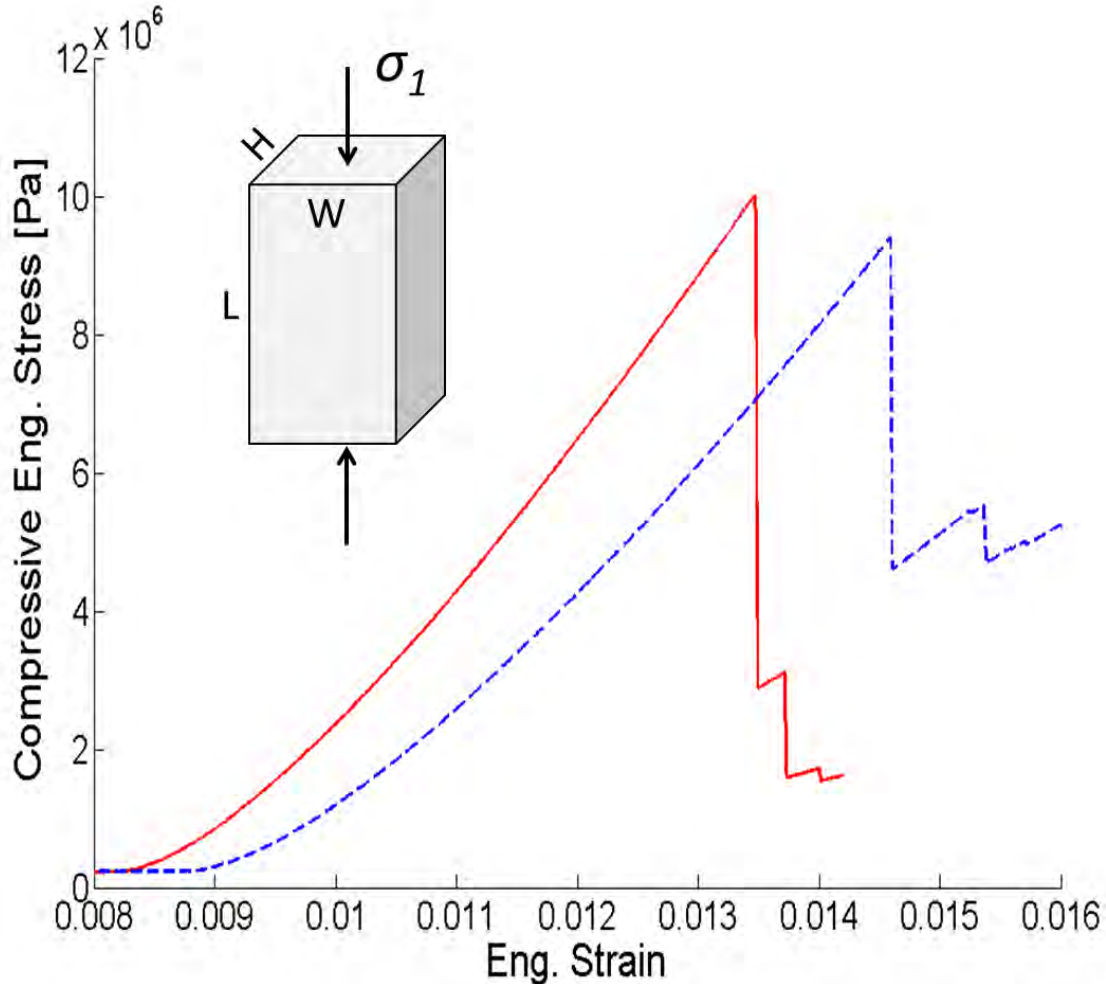


Figure A2. Uniaxial compressive stress-strain curves to failure for two rectangular prisms. Note that for both samples the slope increases monotonically to a constant value before failure indication that damage nucleation and failure occur at the same stress. Sample dimensions were W=4.8mm, H=19.1 mm, and L = 38.1 mm.